

Contents

2	1 Diamond irradiation study	3
3	1.1 Measurement setup	4
4	1.1.1 Preamplifiers	4
5	1.1.2 Diamond samples	6
6	1.1.3 Readout devices	7
7	1.1.4 Setup for the β detection efficiency study	7
8	1.1.5 Room temperature α -TCT setup	8
9	1.1.6 Cryogenic α -TCT setup	8
10	1.2 Charged particle pulses and spectra	9
11	1.3 Radiation limitations	12
12	1.3.1 Irradiation study	12
13	1.3.2 Long-term measurement stability	14
14	1.4 Temperature limitations	22
15	1.4.1 Temperature-variant α -TCT before irradiation	22
16	1.4.2 Temperature-variant α -TCT after irradiation	24
17	1.5 Conclusion	30

¹⁸ **Chapter 1**

¹⁹ **Diamond irradiation study**

²⁰ The aim of the study in this chapter is to find the operational limitations of diamond
²¹ detectors for spectroscopy and tracking applications. The chapter contains the measurement
²² results of data taken with diamond sensors. First the measurement setup is described in
²³ section 1.1. Then the measured particle spectra are shown in section 1.2. This is followed by
²⁴ a study of effects of the irradiation damage on the electrical signal of the diamond detector.
²⁵ The last section shows the results of the measurements of irradiated diamond samples at
²⁶ cryogenic temperatures. The studies compare the experimentally acquired data with the
²⁷ theory from the previous chapter and define limitations of the diamond detectors in terms
²⁸ of radiation and temperature.

²⁹ Diamond sensors are mainly used for two types of measurements: particle counting and
³⁰ spectroscopy. The first type of measurements depends on the sensor efficiency – its ability to
³¹ detect all or at least a known percentage of incident particles. The energy of the particles is
³² not so important; what bears the information is the rate and the spatial distribution. Here
³³ the particles do not necessarily stop in the bulk – they exit the sensor with a slightly lower
³⁴ energy. In spectroscopy, on the other hand, the particles stop within the sensor, depositing
³⁵ all their energy. This energy is then measured by collecting the freed charge carriers. The
³⁶ goal of the experiments described in this chapter is to:

- ³⁷ 1. Quantify the charge collection efficiency of the sCVD diamond in counting mode,
- ³⁸ 2. Quantify the efficiency degradation as a function of fluence,
- ³⁹ 3. Quantify the macroscopic effects on charge carrier behaviour as a function of fluence
and
- ⁴¹ 4. Define limitations for use in spectroscopy.

⁴² The results discussed here show that there are several limitations for using diamond as
⁴³ a radiation detector. All of them need to be taken into account when designing a new
⁴⁴ measurement device. The irradiation study allows for an estimation of the lifetime of the
⁴⁵ detector and a prediction of the longterm signal degradation as a function of fluence. The
⁴⁶ result of the study is a correction factor, which can be applied during data analysis to ensure
⁴⁷ that the analysis results are stable despite the detector degradation.

1.1. MEASUREMENT SETUP

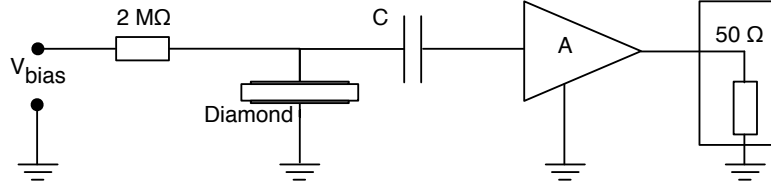


Figure 1.1: Diagram of a diamond detector readout chain.

48 1.1 Measurement setup

49 The first step of designing a measurement setup is to define the measurement conditions,
50 such as temperature, type of radiation and its flux. The second step is to ensure that the
51 setup is insensitive to external electromagnetic interferences and that it minimises electrical
52 noise in the system. The setup needs to be calibrated before use.

53 The measurements using diamond that are explained in these chapters have been carried
54 out using several measurement setups, but they are all similar in terms of the electrical signal
55 chain. The measurement chain consists of three main parts: a diamond sensor, a signal
56 preamplifier and a readout device, as seen in figure 1.1. The preamplifier is capacitively
57 coupled with the diamond. The signals propagating along the analogue chain are in the
58 GHz bandwidth range with amplitudes of the order of tens of μV . This gives rise to the
59 importance of shielding from external radio-frequency (RF) interferences. Also, the carrier
60 and the preamplifier have to have a matched impedance. Finally, the system needs to be
61 grounded properly.

62 1.1.1 Preamplifiers

63 Two preamplifiers are used for the measurements. *CIVIDEC Cx* (figure 1.2a) is a charge sen-
64 sitive amplifier. Its high SNR is achieved due to a low equivalent noise charge of 300 e^- with
65 an additional 30 e^- per each pF of the sensor capacitance. A reported gain of $\sim 12 \text{ mV/fC}$
66 makes it a good choice for spectroscopic measurements with diamond sensors. *CIVIDEC*
67 *C2* (figure 1.2b) [?] is a fast current preamplifier with a 2 GHz bandwidth limit. Both are
68 embedded in an RF-tight aluminium box to reduce the noise pickup. Both have an AC
69 coupled input and a 50Ω output.

70 A 2 GHz bandwidth limit defines the minimum rising time equal to $t_r \simeq \frac{0.34}{BW} = \frac{0.34}{2 \times 10^9} =$
71 170 ps, therefore the system with a CIVIDEC C2 amplifier is capable of measuring pulses
72 with a minimum FWHM $\simeq 170 \text{ ps}$. The initial peak in the α pulse (shown in figure ??) has
73 a lower FWHM; for example, if a positive charge carrier travelling through the bulk takes
74 $t_1 \sim 6 \text{ ns}$ to reach the electrode on the opposite side ($d_1 \sim 500 \mu\text{m}$), the carrier with the
75 opposite charge and a shorter path to the closer electrode – max. $d_2 \sim 10 \mu\text{m}$ – only takes
76 $t_2 \sim \frac{d_2}{d_1} t_1 \times 140 \% = 170 \text{ ps}$ (higher percentage due to slower electron drift). Such a short
77 drift time induces a current pulse that is too narrow for the system to detect.

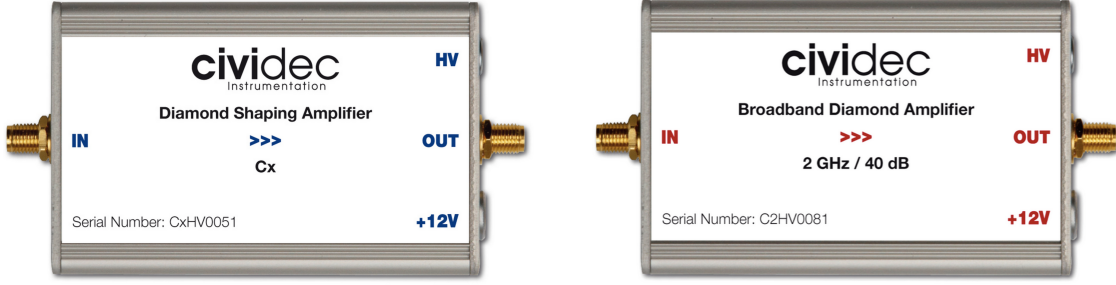


Figure 1.2: CIVIDEC Cx and CIVIDEC C2 amplifiers used for the charge and current measurements.

78 Calibration

79 The amplifiers were calibrated using a square signal generator with a known amplitude step
80 of $U_{\text{in}} = (252 \pm 5)$ mV. A 2 GHz oscilloscope with a 10 GS/s sampling rate was used to
81 carry out the calibration.

82 **Cx charge sensitive amplifier** calibration necessitates an injection of a well known charge.
83 Therefore the signal from a pulse generator is routed through a capacitor with a calibration
84 capacitance $C_{\text{cal}} = (0.717 \pm 0.014)$ pF and then to the input of the amplifier. The pulse
85 area behind the capacitor is $a_{\text{cal}} = (5.0 \pm 0.5)$ pVs, with the signal amplitude on the output
86 amounting to $U_{\text{Cx}} = (1.95 \pm 0.05)$ V. The input voltage step combined with the calibration
87 capacitance yields a calibration charge

$$Q_{\text{cal}} = C_{\text{cal}} \cdot U_{\text{in}} = (181 \pm 5) \text{ fC}. \quad (1.1)$$

88 The gain of the Cx amplifier when comparing the integrated input charge to the output
89 amplitude is

$$A_{\text{Cx}}^{\text{Q}} = \frac{U_{\text{Cx}}}{Q_{\text{cal}}} = (9.3 \pm 0.4) \text{ mV/fC} \quad (1.2)$$

90 whereas the factor between the area of the input current pulse and the output amplitude is

$$A_{\text{Cx}}^{\text{a}} = \frac{U_{\text{Cx}}}{a_{\text{cal}}} = (390 \pm 40) \text{ mV/pVs}. \quad (1.3)$$

91 The area-based amplification factor A_{Cx}^{a} can be used as an estimate for the integrated charge
92 of a current pulse. However, it has a higher uncertainty ($\sim 10\%$) than the amplitude-based
93 factor A_{Cx}^{Q} ($\sim 4\%$) due to the measurement limitations of the oscilloscope.

94 **C2 current amplifier** calibration only requires the measurement of the amplitude gain.
95 To keep the output signal amplitude within the ± 1 V linear range of the amplifier, the
96 input signal amplitude has to be minimised. The signal from the generator is therefore
97 routed through a 36 dB attenuator to decrease its amplitude to $U_{\text{inAtt}} = (3.95 \pm 0.05)$ mV.
98 Two amplifiers with different gains have been measured, because both are used for the

1.1. MEASUREMENT SETUP

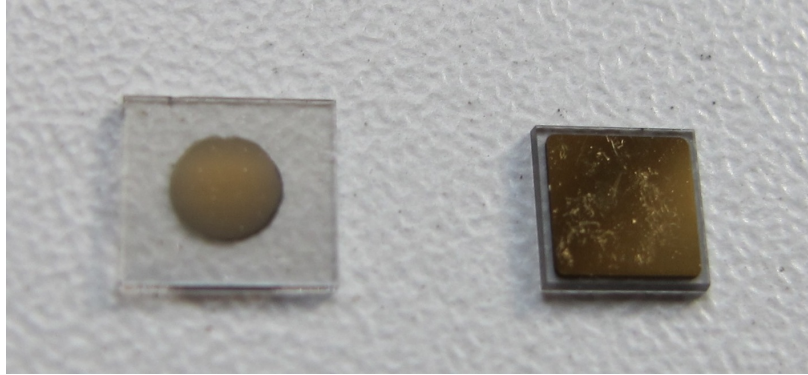


Figure 1.3: Two scCVD diamond samples: A IIa 1scdhq (left) and an E6 S37 (right).

99 measurements. The output of the first amplifier amounts to $U_{C2-1} = (860 \pm 5)$ mV. This
100 yields the amplification gain

$$A_{C2-1} = \frac{U_{\text{inAtt}}}{U_{C2-1}} = (217 \pm 3). \quad (1.4)$$

101 The second amplifier has the output equal to $U_{C2-2} = (632 \pm 5)$ mV with the resulting gain
102 of $A_{C2-2} = (152 \pm 3)$.

103 1.1.2 Diamond samples

104 The sCVD diamond sensor samples used for these studies have been acquired from Element
105 Six (E6) [1]. They all have the same standard dimensions of 4.7×4.7 mm 2 . One sample
106 with dimensions of 5.6×5.3 mm 2 produced by IIa Singapore [2] has also been characterised
107 at CERN [?]. The target thickness for all samples is 500 μm . Table 1.1 shows all diamond
108 samples used for this study. Two of them are measured before and after irradiation and
109 then compared.

Name	Type	Producer	Dimensions [mm 2]	Thickness [μm]	Electrode	Irradiated
S37	sCVD	E6	4.7×4.7	548	Cr/Au	no
S50	sCVD	E6	4.7×4.7	537	Cr/Au	no
S52	sCVD	DDL	4.7×4.7	515	DLC/Pt/Au	$3.6 \times 10^{14} \frac{\pi}{\text{cm}^2}$
			4.7×4.7	529		$1 \times 10^{14} \frac{\pi}{\text{cm}^2}$
S79	sCVD	E6	4.7×4.7	491	Cr/Au	no
ELSC	sCVD	E6	4.7×4.7	460	Cr/Au	no
1scdhq	sCVD	IIa	5.6×5.3		Cr/Au	no

111 Table 1.1: Diamond sensor samples used.

112 The diamond samples have quoted impurity densities of $\leq 2 \times 10^{14}$ cm $^{-3}$ and nitrogen
113 incorporation of $\leq 10^{-9}$ [5]. The electrodes were added by various companies and insti-
114 tutes. For instance, S52 was metallised by a company DDL (now defunct) while the Physics
115 Department of the University of Firenze, Italy metallised the S79. There are also several
116 techniques for producing the electrodes. The DDL contacts consist of three layers: DLC
117 (diamond-like carbon)/Pt/Au with 4/10/200 nm thicknesses, respectively. The metallisa-
118 tion for S79, on the other hand, is made up of Cr/Au with a total thickness of ~ 400 nm.

119 The area coverage also differs from sample to sample. Diamonds must not be metallised
120 until the very edge as the proximity of contacts with a high potential difference may lead
121 to sparking. However, the areas not covered by the metallisation are less efficient because
122 the fringe fields at the edges are not as strong as in between the electrodes. This effectively
123 reduces the sensitive area of the sensors. In the diamonds used here the effective area is
124 anywhere from 9 mm^2 to 18 mm^2 . The leakage current is below 1 nA, but increases for the
125 irradiated samples. The capacitance is of the order of $(2.0 \pm 0.3) \text{ pF}$.

126 1.1.3 Readout devices

127 Electrical signals in diamond detectors are in the GHz frequency range. To preserve the
128 information in the signals, the readout device with a high bandwidth limit must be used.
129 For instance, a 20 MHz limit is enough for the spectroscopic measurements with the Cx
130 charge amplifier, but is insufficient for the current measurements with the C2 amplifier.

131 Two devices are used take data shown in this chapter. The first choice is a 2 GHz LeCroy
132 WaveRunner 204MXi-A. This specific model has a sufficiently high bandwidth limit for the
133 fast current preamplifier signals. It offers a reliable solution for analogue signal readout
134 of limited amounts of data. The second device is DRS4 [4], an analogue data acquisition
135 device developed by PSI, Switzerland, capable of recording up to four waveforms at a time
136 at a steady rate of up to 500 Hz. Its 700 MHz bandwidth limitation is sufficient for the
137 signal from the charge amplifier.

138 1.1.4 Setup for the β detection efficiency study

139 A charge collection efficiency study of the diamond sensors has been carried out at CERN in
140 the North Hall test beam facility. There a straight high-energy particle beam of 120 GeV π
141 is provided to the users to calibrate their detectors. The beam has a transverse spread of
142 $\sigma = 10 \text{ mm}$ in both axes. The particle rate is of the order of $10^4 \pi \text{ cm}^{-2} \text{ s}^{-1}$. A diamond
143 sensor embedded in a printed circuit board (PCB) carrier has been placed in the beam
144 spot perpendicular to the beam and connected via an SMA connector directly to a charge
145 sensitive amplifier. The amplified signal is read out using a LeCroy oscilloscope and a
146 DRS4 analogue readout system. A computer is used as a controller and data storage for
147 the readout device. A beam telescope is used as a reference detector. It is a device that
148 helps to cross-check the measurements of the devices under test (DUTs) and to carry out
149 spatially resolved studies on the DUTs. It consists of several pixellated sensor planes placed
150 in series, which can track a particle's trajectory with a precision of a few μm . The sensor
151 planes are positioned in front of the DUT and behind it. Then the beam telescope acts as
152 a trigger system – it triggers the readout of both the telescope data and DUT data when
153 both the planes in front and behind the DUT record a hit by an incident particle. A particle
154 detected by all the planes within the DUT window and the DUT itself counts towards its
155 efficiency whereas a hit missed by the DUT means that the DUT is not 100 % efficient. To
156 discard the hits that miss the DUT completely, a region of interest (ROI) can be chosen in

1.1. MEASUREMENT SETUP

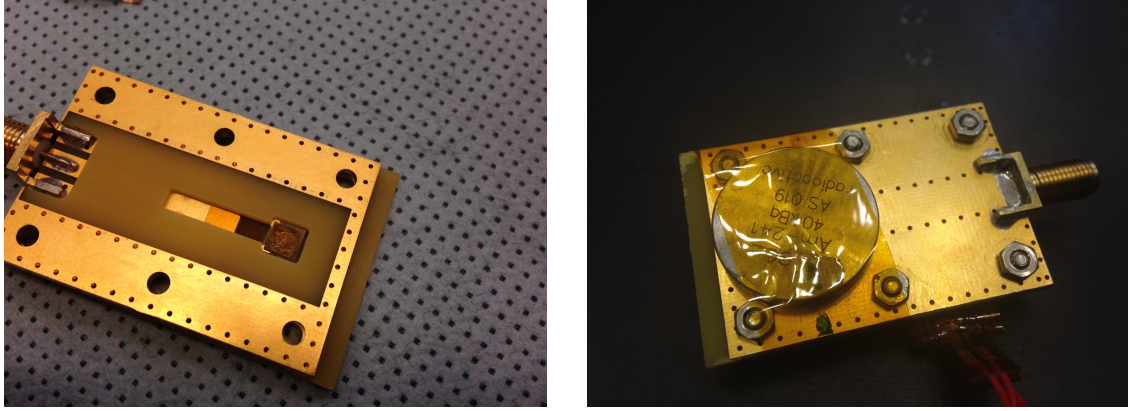


Figure 1.4: Positioning of the α -source on top of the sensor carrier.

157 the beam telescope planes. The equation for calculating the sensor efficiency is therefore

$$\epsilon = \frac{N_{\text{DUT}} \wedge N_{\text{telescope}}}{N_{\text{telescope}}} \quad (1.5)$$

158 for an ROI smaller than the sensitive region of the diamond.

159 1.1.5 Room temperature α -TCT setup

160 Room-temperature TCT measurements have been carried out in the laboratory. The setup
161 consists of a diamond sensor embedded in a PCB carrier, a current amplifier and an oscillo-
162 scope. To measure α particles, their energy loss during their trajectory has to be minimised.
163 Therefore the diamond is placed inside a vacuum chamber. The chamber is a steel tube
164 with a diameter of 5 cm. On one side it is connected to a vacuum pump via a steel hose. A
165 feedthrough with an SMA connector is placed on the other side. A CIVIDEC C2 current
166 amplifier is connected directly onto the feedthrough. The amplified output is connected
167 to the oscilloscope via an SMA cable. An ^{241}Am source with a diameter of 2 cm and a
168 height of 0.5 cm is fixed onto the sensor carrier (figure 1.4a, figure 1.4b). Then the carrier
169 is inserted in the chamber and fixed in place using an air-tight clamp. The pump can then
170 be switched on. It is capable of providing an inside pressure as low as 10^{-4} mbar after
171 approximately one hour of operation.

172 1.1.6 Cryogenic α -TCT setup

173 This TCT study is a follow-up of an extensive diamond TCT study at cryogenic temper-
174 atures [5]. The experiment at cryogenic temperatures has been carried out at the Central
175 Cryogenic Laboratory at CERN. The room-temperature TCT setup has to be modified to
176 allow for measurements at temperatures as low as 4 K. It consists of three parts:

- 177 1. a cryostat – a thermally insulated cylinder containing liquid helium,

- 178 2. an inlet – an air-tight mechanical tube with valves and feedthroughs at the top that
179 is lowered in the liquid helium and

180 3. a diamond sample embedded in a PCB carrier with a fitted temperature sensor, a
181 heater and cables leading to the feedthroughs.

182 The setup is described in detail in [5].

183 When the diamond sample is placed in the PCB carrier and the ^{241}Am source is in
184 place, the inlet is sealed and lowered in the empty cryostat. Then the inside volume of the
185 inlet is evacuated down to 10^{-5} mbar while the liquid helium is flowing into the cryostat.
186 To improve the thermal contact between the diamond and the coolant, a small amount of
187 helium gas is added inside the evacuated inlet, setting the vacuum to around 10^{-3} mbar.
188 This value changes with time, because the gas condenses on the walls of the inlet, reducing
189 the number of floating particles. For this reason the helium gas has to be added on an
190 irregular basis. Every addition causes a significant undershoot of the sample temperature,
191 which has to be corrected for using a heater placed on the back of the PCB carrier. Also,
192 the added gas deteriorates the vacuum inside the inlet. Furthermore, at approximately 60 K
193 the helium gas has to be evacuated from the inlet to avoid a potential explosion due to the
194 expansion of the gas with temperature.

195 When the sample is cooled to 4 K, the minimum temperature achievable by means of
196 liquid helium without over-pressurising it, the measurements can begin. A temperature
197 sensor placed on the back of the PCB carrier is used to measure the temperature of the
198 sample. After every measurement, the current through the heater is increased, heating up
199 the sample to the next temperature point. The initial temperature time constant of the
200 order of tenths of seconds at low temperatures increases with temperature. Even more so
201 when helium is evacuated from the inlet at 60 K, removing the thermal bridge between
202 the wall of the inlet and the diamond sample. At the room temperature (RT), the time
203 constant is already of the order of minutes.

204 1.2 Charged particle pulses and spectra

205 In previous chapter the ionisation profiles for different types of radiation were discussed.
206 A β particle induces a triangular electric pulse whereas a pulse induced by an α particle
207 is rectangular. However, their amplitude, width and rise/fall time depend heavily on the
208 type of interaction with the diamond, the purity of the diamond and the bandwidth of the
209 amplifier and the oscilloscope. This section shows the signal pulses of α , β and γ radiation
210 with their respective energy distributions for the case of a diamond detector.

211 Figure 1.5 shows a set of pulses and an averaged waveform for 5.5 MeV α , 2.3 MeV
212 β and 1.3 MeV γ radiation using an ^{241}Am , a ^{90}Sr and a ^{60}Co source, respectively. The
213 particles are measured with the non-irradiated SCVD diamond S37. α particles always
214 produce the same signal pulse with a noise RMS of 2.7 mV. The averaging suppresses the
215 noise while retaining most the information. It does, however, smear the rising and falling
216 edge, increasing the rising and falling time. The t_r is now of the order of 0.5 ns. The pulse

1.2. CHARGED PARTICLE PULSES AND SPECTRA

217 count for β and γ is low, so the pulses with a high amplitude are not recorded. A trigger
218 would need to be set very high to “catch” them with the oscilloscope. Both β and γ pulses
219 look similar - triangular and with a wide range of amplitudes.

220 Histograms on the right hand side of figure 1.5 show distributions for of deposited charge
221 as measured with a CIVIDEC Cx amplifier. The distribution of α particles is a Gaussian
222 while the β distribution follows a Landau function. γ distribution should look the same as
223 β , but is different. This is because the γ data were taken with a self-trigger set to 20 mV
224 rather than an external trigger. Therefore the distribution includes signals from scattered
225 particles and noise contributions.

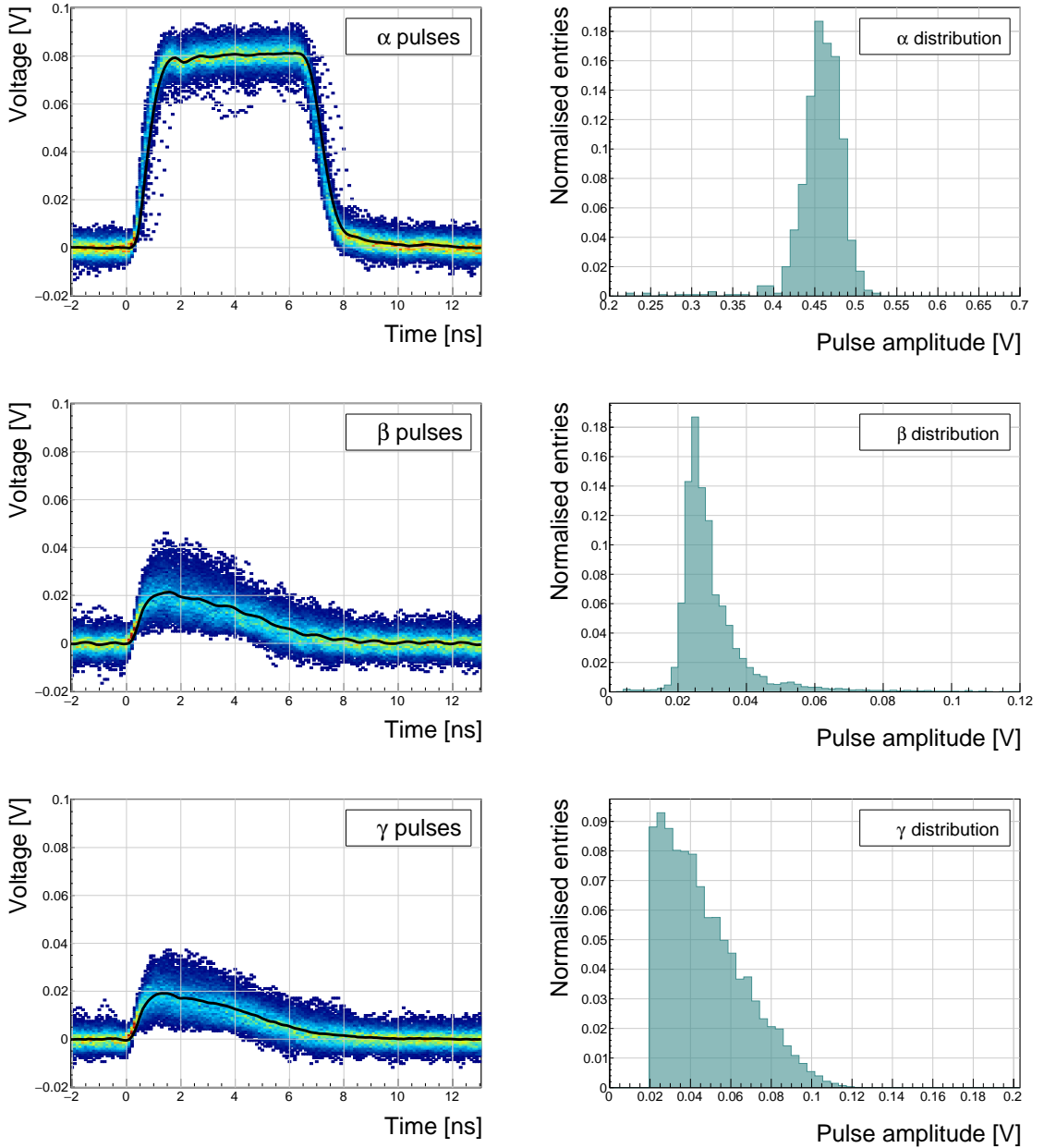


Figure 1.5: Superimposed and averaged pulses (left figures, current amplifier) and distributions of deposited energy (right figures, charge amplifier) for three types of radiation. Note the scale on the x axis of the distributions.

²²⁶ **1.3 Radiation limitations**

²²⁷ This section quantifies the decrease in charge collection efficiency as well as the effects on
²²⁸ long-term measurement stability in irradiated sCVD diamonds.

²²⁹ **1.3.1 Irradiation study**

²³⁰ This subsection contains a study of the effects of 300 MeV pion irradiation on the charge
²³¹ collection efficiency of sCVD diamond detectors. To carry out this study, two diamond
²³² samples were irradiated with 300 MeV pions (π , kinetic energy 191.31 MeV). The irradiation
²³³ campaign took place at the Paul Scherrer Institute (PSI) [6] where the machine provides
²³⁴ a flux of $1.5 \times 10^{14} \pi \text{ cm}^{-2}$ per day. The quoted uncertainty on the measurement of the
²³⁵ delivered dose is $\pm 20\%$. In addition, a deviation in beam energy can have a significant
²³⁶ effect on the damage in the sensor, considering the pion damage curve in figure ?? at a
²³⁷ $\pi_{300 \text{ MeV}}$ point (191 MeV kinetic energy), which sits on a steep section of the DPA curve.
²³⁸ The target fluences for S79 and S52 were $(1 \pm 0.2) \times 10^{14} \pi \text{ cm}^{-2}$ and $(3.6 \pm 0.7) \times 10^{14} \pi \text{ cm}^{-2}$.

²³⁹ A test beam campaign was carried out to observe the charge collection efficiency at
²⁴⁰ different bias voltage settings. The efficiency values acquired are used to determine the
²⁴¹ effective drop in efficiency as a function of fluence. This is to test if the collected charge
²⁴² Q is inversely proportional to the fluence Φ , as per equation ?? . A procedure defined by
²⁴³ a collaboration researching diamond behaviour RD42 has been applied to the measured
²⁴⁴ values to extract the damage factor described in section ??.

²⁴⁵ Subsection 1.3.2 contains measurements and results of a long-term stability study using
²⁴⁶ α and β particles. In particular, charge collection efficiency with β and α radiation as a
²⁴⁷ function of time is measured. To investigate the effect of decreased charge collection of
²⁴⁸ irradiated diamond with time, TCT (transient current technique) is employed. Finally, a
²⁴⁹ procedure that improves the pulse shapes and the charge collection efficiency is proposed.

²⁵⁰ **300 MeV π radiation damage factor**

²⁵¹ Three diamonds – non-irradiated S37 and irradiated S52 and S79 – were tested in a $\pi_{120 \text{ GeV}}$
²⁵² test beam in the SPS North Experimental Area at CERN [7] before and after irradiation.
²⁵³ The goal was to estimate the charge collection efficiency and charge collection distance as a
²⁵⁴ function of fluence. The samples were primed prior to data taking using a ${}^{90}\text{Sr}$ radioactive
²⁵⁵ source. The data were then taken at a range of bias voltages ranging from 30 V to 900 V,
²⁵⁶ yielding between $0.06 \text{ V}/\mu\text{m}$ and $1.8 \text{ V}/\mu\text{m}$ electrical field in the bulk. Every data point
²⁵⁷ contained approximately 5×10^4 measured particles. The charge deposited by the particles
²⁵⁸ was measured using a CIVIDEC Cx charge preamplifier.

²⁵⁹ The integrated amplitude spectrum is a Landau distribution. Its most probable value
²⁶⁰ (MPV) is used to calculate the most probable collected charge Q_i :

$$Q_i [\text{e}^-] = \frac{1}{1.6 \times 10^{-19}} Q_i [\text{C}] = 6'241 \cdot Q_i [\text{fC}] = 6'241 \cdot \frac{\text{MPV} [\text{mV}]}{A [\frac{\text{mV}}{\text{fC}}]}, \quad (1.6)$$

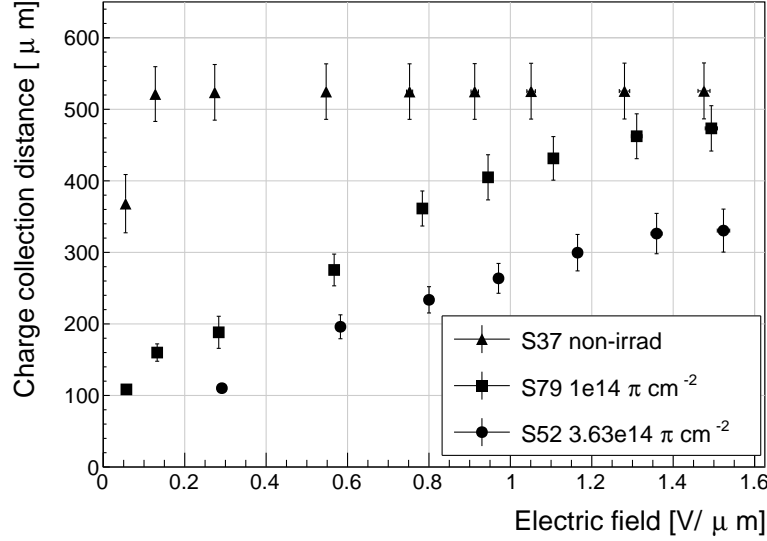


Figure 1.6: The figure shows the CCD for S37, S79 and S52 at a range of bias voltage settings.

where $A = 9.3 \text{ mV/fC}$ is the preamplifier gain factor and $1 e^- = 1.6 \times 10^{-19} \text{ C}$.

The CCD for the three measured samples at a bias voltages ranging from $0.2\text{--}1.6 \text{ V } \mu\text{m}^{-1}$ calculated using equation ?? is shown in figure 1.6. S37 exhibits a full collection distance already at $0.4 \text{ V } \mu\text{m}^{-1}$ whereas the irradiated samples have a more gentle increase of CCD with increasing bias voltage. It is evident that at $1 \text{ V } \mu\text{m}^{-1}$ the maximum CCD has not been reached in the case of S79 and S52. Nevertheless, to compare the measured data point with those provided by RD42, the CCD at $1 \text{ V } \mu\text{m}^{-1}$ has to be taken.

Data points with the maximum CCD obtained in the test beam measurements are plotted as a function of fluence in figure 1.7. Equation ?? is fitted to the data points and a damage factor $k_\lambda = (4.4 \pm 1.2) \times 10^{-18} \text{ } \mu\text{m}^{-1} \text{ cm}^2$ is obtained. The value is for a factor of two higher than the damage factor obtained by RD42. This could be due to an insufficient priming time ahead of the measurement. The samples were only exposed to the radioactive source for a short time and might not have achieved the maximum charge collection (effect of priming shown in figure 1.8). In addition, the diamond samples have not been polished and re-metallised after irradiation, as is the case for the RD42. A study of effects of re-metallisation on the charge collection has been done in [8] and supports this theory. Furthermore, with only two samples measured, the statistical uncertainty is high. For a better fit another measurement point at a higher fluence would need to be added. Nevertheless, it can be concluded that the 300 MeV pions damage the diamond bulk significantly more than the 24 GeV protons, as shown in chapter ??.

Another diamond irradiation study has been carried out using the Beam Conditions Monitor (BCM) at the CMS experiment [?]. The BCM's diamond sensors have been exposed to radiation from beam collisions with a wide spectrum of energies and particle types. The

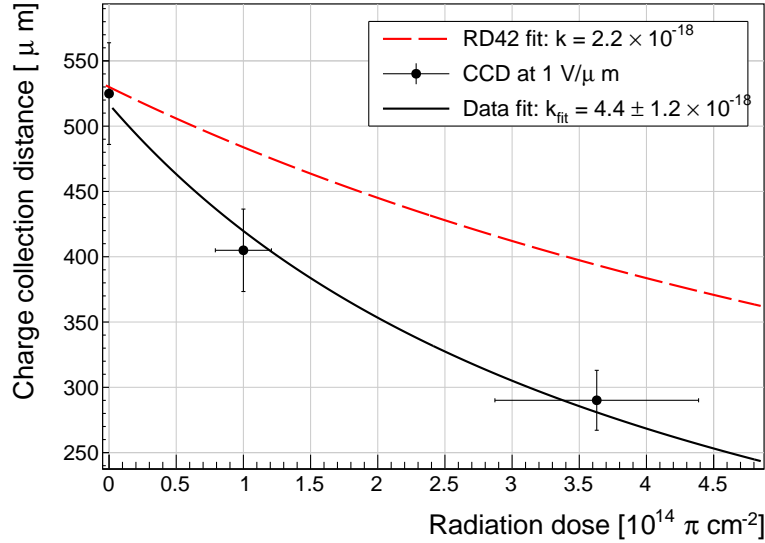


Figure 1.7: The charge collection distance at 1 V/ μm bias voltage for the three diamond samples is plotted as a function of fluence. It is compared to the RD42 data for pion irradiation. The data points are about 15–25 % lower than expected from the RD42 data [9].

284 damage factors measured are an average of $3.5 \times 10^{-17} \mu\text{m}^{-1} \text{cm}^2$ and $9.2 \times 10^{-16} \mu\text{m}^{-1} \text{cm}^2$
 285 for pCVD and sCVD diamonds, which is for a factor of 58 and 1500 higher than the RD42.
 286 These low charge collection efficiencies, however, are purported to be convoluted with other
 287 effects, such as polarisation, which will be discussed later in the chapter.

288 1.3.2 Long-term measurement stability

289 An important requirement for particle detectors is a stable performance over long periods
 290 of time. For instance, charge collection for a defined radiation type and quantity must not
 291 change over time or has to change in a predicted way. The stability of diamond detectors
 292 depends on many factors, e.g. material purity, polishing process, electrode material, irradia-
 293 tion damage etc. The aim is to study the behaviour of diamond under controlled conditions,
 294 with the goal to understand its limitations. One of these limitations is the fluence as it can
 295 affect the long-term stability of the sensor during operation.

296 The three diamond samples (S37, S79 and S52) have been exposed to two different types
 297 of ionising radiation for a longer period to see if their behaviour changes over time. Two
 298 parameters have been observed in particular:

- 299 1. Charge collection of β particles and
 300 2. Charge collection and ionisation profile of α particles.

301 **β long-term stability**

302 The diamond samples have undergone a long-term stability test at room temperature using
303 β radiation. This has been done using a ^{90}Sr source emitting ~ 2.28 MeV electrons at a
304 rate of approximately $10^4 \text{ e}^- \text{ cm}^{-2} \text{ s}^{-1}$ as measured using a real-time particle counting
305 application described in chapter ???. To simulate the initial conditions in HEP experiments,
306 the sensors must not be primed before starting the measurements. The measurement setup
307 consists of a diamond sample (S37, S52 or S79) with the CIVIDEC Cx spectroscopic am-
308 plifier, a silicon diode with a CIVIDEC C6 amplifier for triggering and a ^{90}Sr source on
309 top. A particle emitted by the source traverses the sensor bulk and hits the silicon diode,
310 triggering the analogue signal readout. The source is left on the top for the course of the
311 experiment. The measurements, however, are taken at discrete times. For every data point,
312 approximately 10^4 triggers have to be recorded. The offline analysis of the recorded signal
313 pulse amplitudes yields a Landau distribution for every data point. The current charge
314 collection relative to the initial charge collection for every sample is plotted as a function
315 of the received β dose in figure 1.8. It shows that, for the irradiated samples, the charge
316 collection efficiency improves when the diamond sensor is primed with a β source. The
317 effect is negligible for the non-irradiated high-quality S37. Both relative increases are sig-
318 nificant – 22 % for S79 and 55 % for S52. At a fluence of approximately 4×10^6 particles
319 the charge collection is stabilised. At that point S79 achieves close to a full efficiency (in
320 absolute values – not shown) whereas S52 reaches approximately 50 %.

321 To sum up, diamond provides a stable measurement of the β radiation detection after
322 reaching a stable state. Even if damaged by radiation, it reaches a stable charge collection
323 at a fluence of $\sim 4 \times 10^6$ MIPs. Its efficiency decreases with a high fluence. However, the
324 decrease can be accounted for if the damage factor and the rate and energy of the particles
325 are known. γ radiation has a similar impact on the diamond as the β . The incident
326 photons, if they interact with the diamond, prime the bulk, increasing the charge collection
327 efficiency. The difference, however, is that the interaction probability (cross-section) is lower
328 for gammas [10, 11].

329 **α long-term stability**

330 This part discusses the stability of irradiated diamond sensors during α measurements. An
331 ^{241}Am source has been used, emitting α particles with a mean energy of 5.5 MeV with an
332 average rate of 7 s^{-1} .

333 To test the stability of the diamond during α measurements, the samples have been
334 biased at +500 V and exposed to up to 8×10^3 α hits while measuring their charge collection
335 efficiency using the CIVIDEC Cx spectroscopic amplifier. The charge collected at every
336 measurement point $Q(\Phi)$ is compared to collected charge of the first measurement $Q(0)$.
337 The resulting ratio $\frac{Q(\Phi)}{Q(0)}$ for all samples is shown in figure 1.9. Each measurement point is
338 an average of 30 consecutive α hits. The observations are the following:

- 339 - $Q(\Phi)$ for the non-irradiated S37 is stable as compared to $Q(0)$ over the course of the
340 measurement.

1.3. RADIATION LIMITATIONS

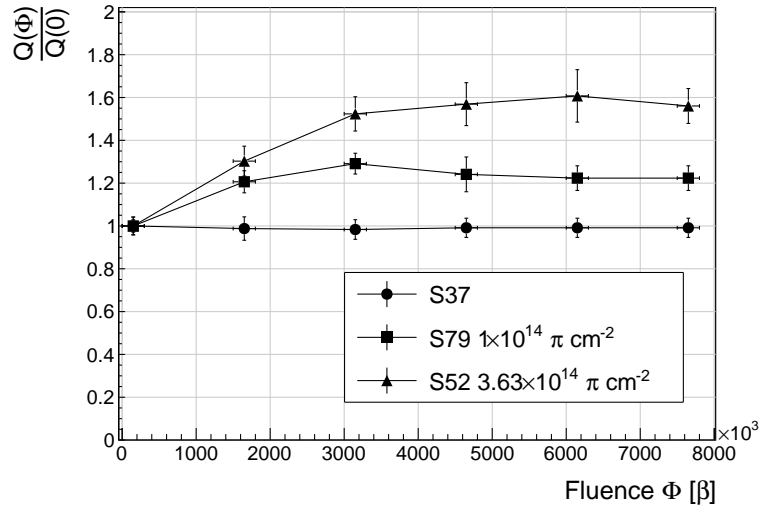


Figure 1.8: Relative increase of charge collection over time due to priming with the ^{90}Sr radioactive source. The charge collection for the non-irradiated S37 stays constant. The bias voltage for this measurement is $1 \text{ V}/\mu\text{m}$.

- The initial efficiency of the irradiated S52 and S79 starts decreasing already at a low α count.
 - The charge collection efficiency of the unprimed irradiated samples drops much faster than after priming.
 - The particle count rate decreases with decreased efficiency, which is clearly seen in the unprimed S52 data where the data points at a low efficiency are much further apart.
- The absolute values are not shown here because only the relative drop is of interest in the scope of the long-term stability tests.

To investigate this sudden drop in efficiency, the current pulse shapes using a CIVIDEC C2 current amplifier have to be observed, as shown in figure 1.10. The shape of the pulse holds more information about the charge carrier properties in the sensor than solely the value of the integrated charge. This time only the primed S79 sample has been tested. Both the hole and the electron collection are observed to determine whether they behave differently or not.

The first observation in the raw acquired data in figures 1.10 is that the initially stable pulses start deteriorating; several different shapes start appearing gradually, some still very similar to those from the beginning while the others with almost zero amplitude.

A more dedicated analysis of the first observation has been carried out as follows: at the beginning of the test when the diamond is still operating stably, 60 pulses are recorded. An average pulse is calculated. This is a reference pulse for the subsequent measurement points. Then an RMS of the individual pulses σ_n with respect to the reference pulse is

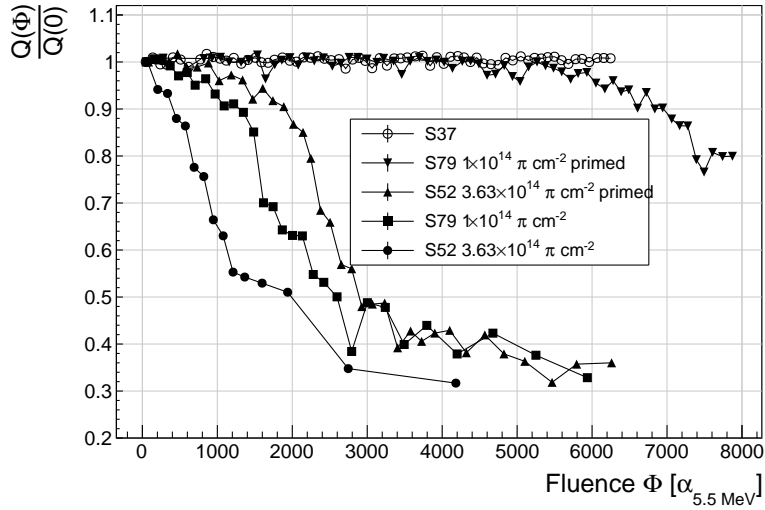


Figure 1.9: A relative drop in charge collection efficiency as a function of the received α dose for non-irradiated and irradiated diamond samples.

362 calculated and the resulting RMS values are summed together into $\sigma(0)$:

$$\sigma(0) = \sum_{n=1}^{60} \sigma_n. \quad (1.7)$$

363 All the subsequent data points also consist of a set of 60 pulses. At every data point the
 364 summation of the RMS values of the individual pulses with respect to the initial averaged
 365 pulse σ is calculated according to equation 1.7. The ratio between the initial $\sigma(0)$ and
 366 discrete values σ gives a measure of the change of the pulse shape with respect to the
 367 reference pulse at the start of the measurement. Therefore the initial value is 1 and it
 368 decreases if the RMS values of subsequent data points are higher. Figure 1.11 shows the ratio
 369 $\frac{\sigma(\Phi)}{\sigma(0)}$. From the data obtained it can be concluded that the initial pulse shape quickly starts
 370 deteriorating. In fact, the deterioration of the shape follows an approximate exponential
 371 decay function before it settles at the lowest value. The resulting decay constants for
 372 electrons and holes are $\tau_e = (4400 \pm 150) \alpha^{-1}$ and $\tau_h = (3300 \pm 140) \alpha^{-1}$. The electrons
 373 retain the initial shape for longer. The deteriorated shapes also seem to be for a factor of
 374 2 better than those of the holes.

375 **Discussion** One hypothesis is that this behaviour is caused by space-charge build-up.
 376 Charge carriers get stopped in the charge traps in the bulk for a long time, building up
 377 regions of space-charge. The built up space-charge creates an internal electric field – po-
 378 larisation. This field in turn affects the speed of the drifting charge carriers. Since the
 379 movement of the carriers is inducing the electric current, the field gradient can be observed
 380 in the current signal. The fact that the signal shapes vary significantly might be due to a
 381 very non-uniform electric field, suggesting a complex polarisation in the sensor.

1.3. RADIATION LIMITATIONS

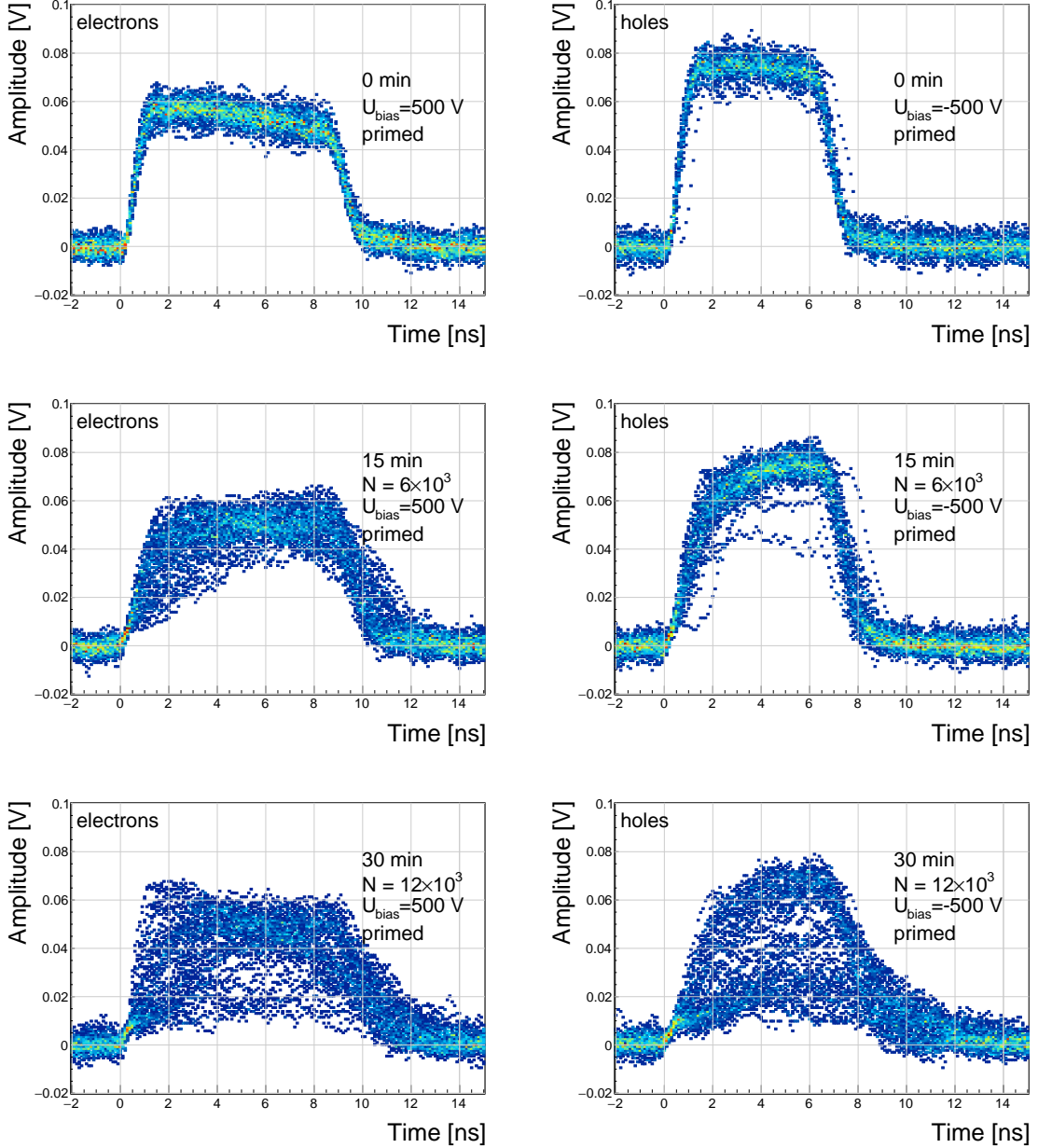


Figure 1.10: The signal of the irradiated and primed S79 deteriorates with time for both polarities. Every plot contains 60 superimposed pulses.

382 Figure 1.12 shows how the space-charge might be built up at the entry point of the α particle.
 383 The assumption is that the first few μm of diamond surface are significantly more damaged
 384 than the rest of the material. Therefore the probability that charge carriers would get
 385 trapped at the edge of the sensor is higher. If the sensor is biased as shown in the figure,
 386 the positive charge cloud drifts towards the adjacent electrode while the negative cloud
 387 drifts through the sensor to the opposite one. Therefore most of the trapped carriers at the
 388 adjacent electrode are positive, forming a strong positive space-charge barrier in the first few

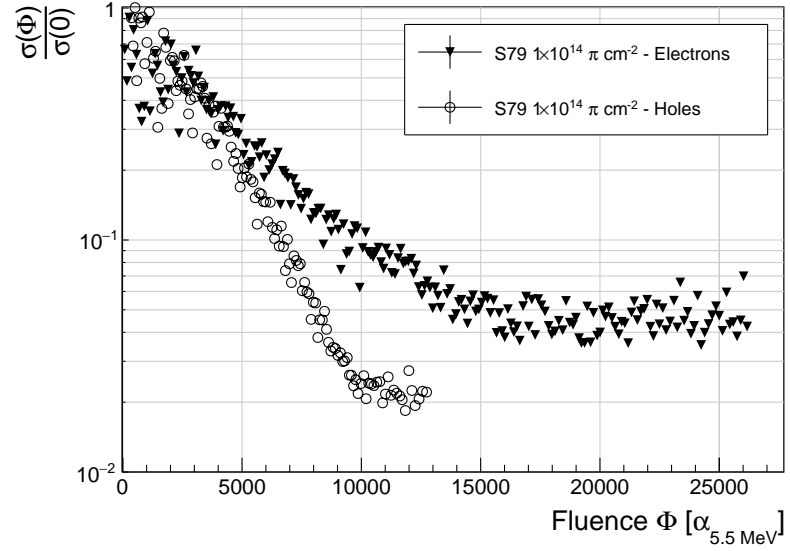


Figure 1.11: Deterioration of the pulse shapes with time.

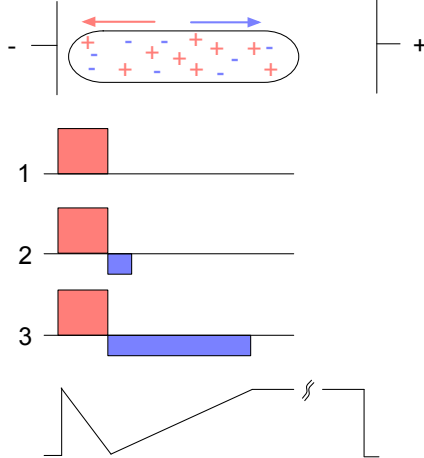


Figure 1.12: Space-charge build-up at the electrode.

389 μm of the sensor (1). The negative carriers created by subsequent α particles are attracted
 390 by the positive space charge and get trapped close to the positive space-charge (2). This
 391 negative space-charge region is gradually stretched inwards (3). Together the two regions
 392 form a barrier which counteracts the externally applied electrical field. Such a distortion
 393 of the field prevents the charge carriers from drifting freely within the space-charge region.
 394 Only those negative carriers that diffuse through this barrier can start drifting towards the
 395 positive electrode. Others either recombine or are trapped, contributing to the build-up of
 396 the barrier.

397 This hypothesis explains the gradual loss of collected charge in figure 1.9 and the pulses

1.3. RADIATION LIMITATIONS

398 with a slow rising edge in figures 1.10. However, it cannot explain the electron pulses
399 with a negative slope. Further reading regarding the space-charge build-up is available
400 in [12, 13, 14], however, no direct explanation of the observed phenomenon has been given.

401 **Restoring the pulse shapes** Finally, an effort has been made to find a way for the pulse
402 shapes to return to their initial state. Five methods are listed:

- 403 1. No source, with bias voltage,
- 404 2. No source, without bias voltage,
- 405 3. Priming with γ at a rate of $400 \text{ s}^{-1}\text{cm}^{-1}$ without bias voltage,
- 406 4. Priming with β at a rate of $1'000 \text{ s}^{-1}\text{cm}^{-1}$ with bias voltage and
- 407 5. Priming with β at a rate of $1'000 \text{ s}^{-1}\text{cm}^{-1}$ without bias voltage.

408 Before starting each method, the diamond sample S79 is first primed using a ^{90}Sr source for
409 approximately one hour. Then the bias voltage is switched on and an ^{241}Am source is put
410 on top. The pulses produced by the incident α particles have a proper rectangular pulse
411 at the beginning, but then start changing – first gradually and later increasingly more in
412 an erratic way, as described in the text above. After approximately 30 minutes, one of the
413 methods is tested. When a “healing” procedure is started, a set of 60 pulses is taken at
414 irregular points of time to observe the change in the pulse shape and to assess the quality
415 of the “healing” procedure. Then the bias voltage is switched off and the sample is primed
416 again to reset its state before starting the next measurement.

417 The results depicted in figure 1.13 show that the methods (3) and (5) improve the shape,
418 method (2) helps slowly, (1) does not show any change with time and (4) at first improves,
419 but then significantly degrades the shape. The effect observed in method (4) has already
420 been described in [15]. The “healing” process therefore depends on the rate of radiation,
421 the bias voltage and the time of exposure. The ionising radiation creates free charges, which
422 quickly recombine close to the place of generation. It is likely that they also release the
423 charges trapped during the measurement, reducing the overall effect of the space-charge.
424 The traps get filled with both flavours of carriers, thus they are neutralised. The pulse
425 shape gradually returns to its initial state.

Procedure	Source	Type of radiation	Bias voltage	Effectiveness
1	/	/	ON	no
2	/	/	/	slow
3	^{60}Co	γ	/	YES
4	^{90}Sr	β	ON	no
5	^{90}Sr	β	/	YES

427 Table 1.2: Effectiveness of healing procedures.

428 **Summary** The shape of the pulses caused by α radiation changes with time for irradiated
429 samples. The shape of the pulses gets distorted. The charge collection decreases and its
430 spread increases. The signal shapes are probably affected by a non-uniform electric field,
431 which is caused by polarisation in the sensor. The signal degradation happens even faster

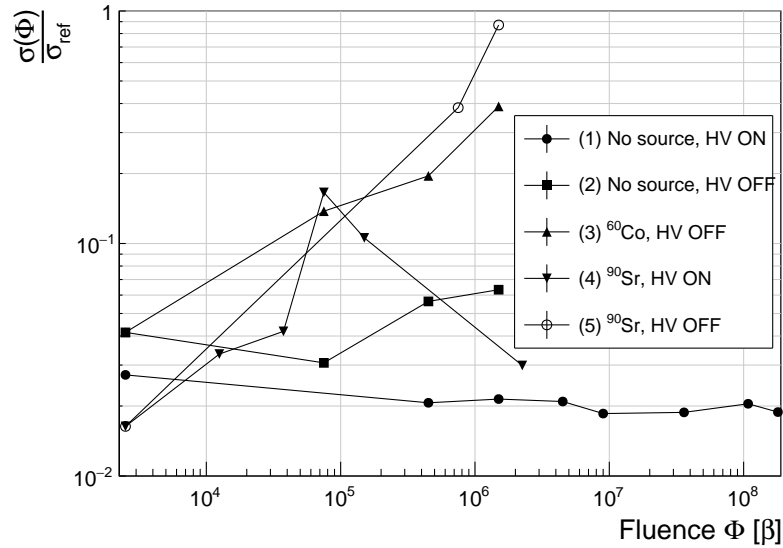


Figure 1.13: Comparison of the five procedures for the “healing” process for an irradiated diamond that had been exposed to α radiation with a rate of 7 s^{-1} , with the bias voltage switched on, for at least 30 minutes.

432 for non-primed diamonds. To “heal” the diamond – to bring the pulse shapes back to their
 433 initial shape – the sample must be primed using a β or a γ source for several minutes
 434 without bias voltage. Switching to the inverse polarity for a few seconds helps a bit, but in
 435 a long run distorts the signal, preventing it from returning to the initial shape.

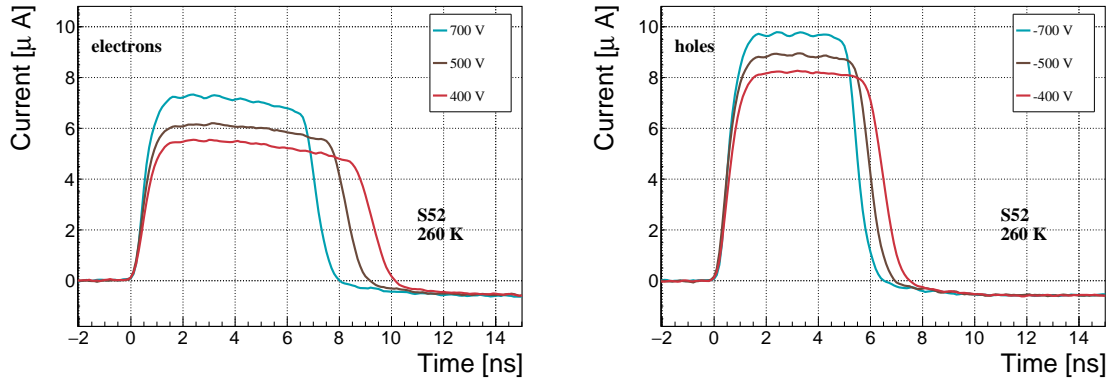


Figure 1.14: Varied bias voltage at a fixed temperature of 260 K.

436 1.4 Temperature limitations

437 A test has been carried out to evaluate the effect of temperature on the output signal of
 438 the diamond sensors. A cryostat filled with liquid helium is used to cool down the sensor
 439 during the measurement process. The current signal response to α -particles is measured at
 440 18 temperature points between 4 K and 295 K. At every temperature point a set of 300
 441 pulses is recorded at a range of positive and negative bias voltages and averaged in the
 442 analysis.

443 1.4.1 Temperature-variant α -TCT before irradiation

444 Three sCVD diamond samples have been tested at a range of temperatures using the α -
 445 TCT technique to verify the consistency of the results with those obtained by H. Jansen
 446 in [5].

447 The resulting averaged pulses of the non-irradiated sample S52 at the 260 K temperature
 448 point and a bias voltage of ± 700 V, ± 500 V and ± 400 V are shown in figure 1.14. The
 449 pulses induced by positive charge carriers are shorter than those induced by electrons, which
 450 means that holes travel faster in diamond. The area of the pulse, however, is the same for
 451 both polarities, which corresponds to the fact that the same amount of charge carriers is
 452 drifting in both cases.

453 Figure 1.15 shows pulses at a bias voltage set to ± 500 V across the range of tempera-
 454 tures between 4 K and 295 K. Several conclusions can be drawn by observing their shape.
 455 First, the pulse shapes change with decreasing temperature. The pulse time gets shorter
 456 and higher, hinting at the faster carrier drift velocity v_{drift} . Second, between 150 K and
 457 75 K there is a significant change in shape – the time constant of the rising edge increases
 458 significantly and the pulse area decreases [5]. From 75 K down to 4 K there is no significant
 459 change. Last, the top of the pulse at the S52 is not flat, which means that a portion of
 460 the drifting charge is lost along the way. This is due to the built up space-charge, likely by
 461 means of crystal defects or impurities introduced during production.

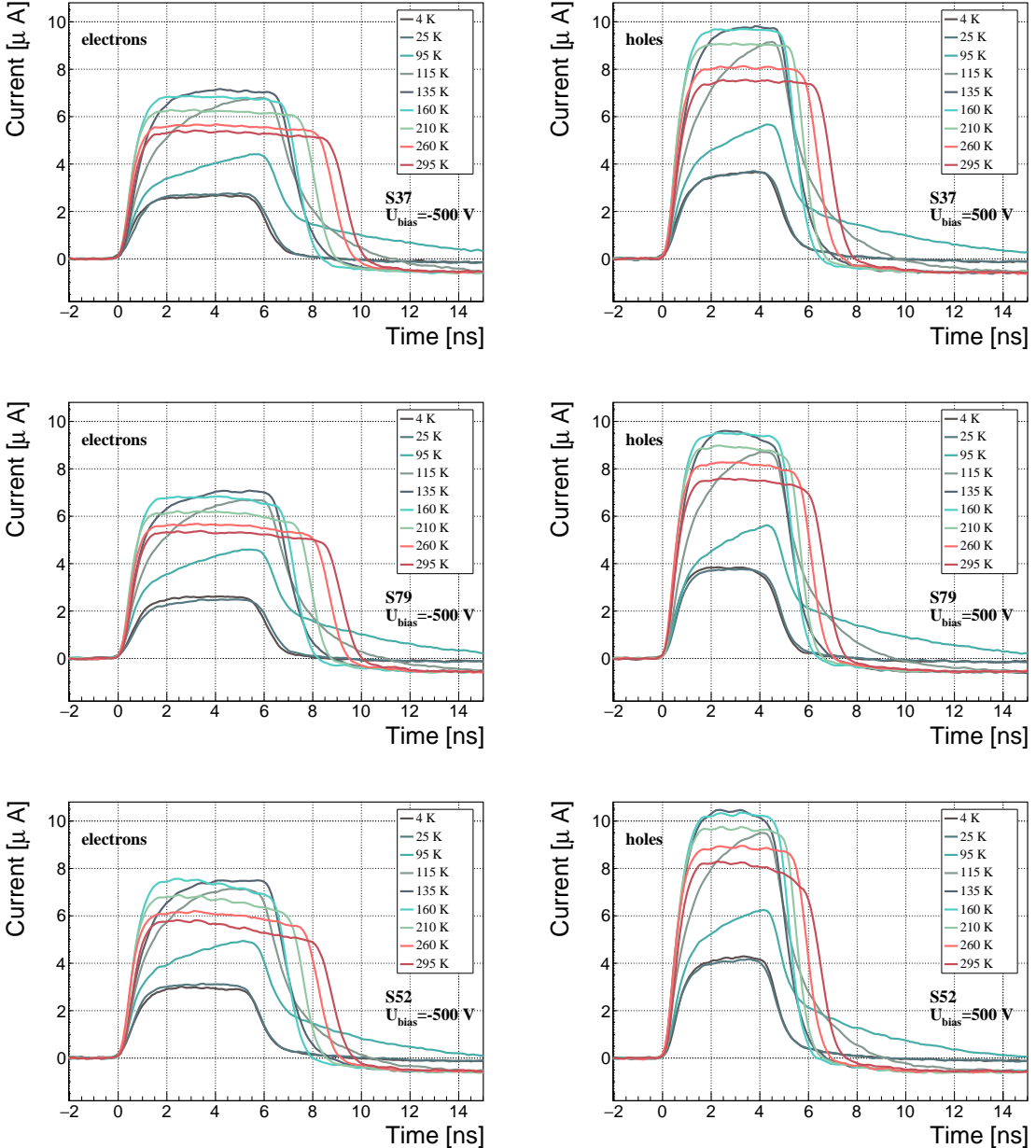


Figure 1.15: Three non-irradiated diamond samples: S37, S79 and S52. Several data points between 4 K and 295 K at a bias voltage of ± 500 V (electrons and holes). The tilted top of the pulse on the bottom left figure is due to built-up space charge.

1.4. TEMPERATURE LIMITATIONS

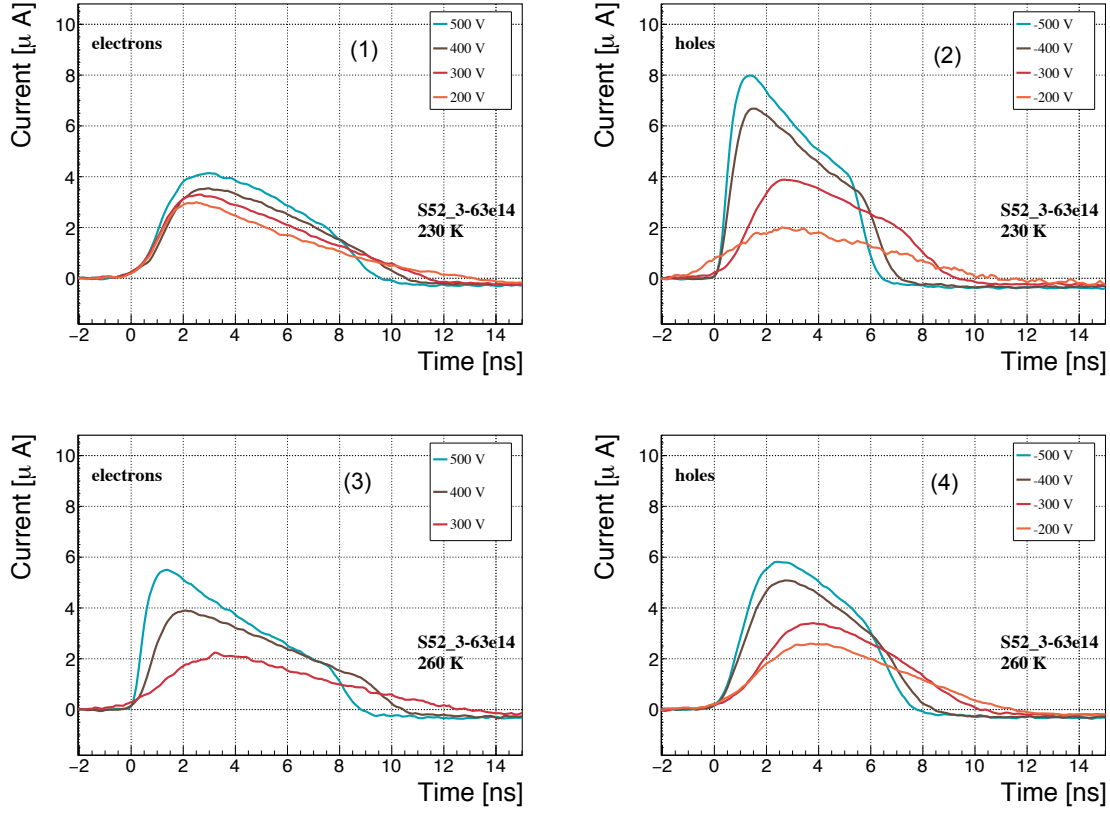


Figure 1.16: Varied bias voltage at a fixed temperature for an irradiated sample.

1.4.2 Temperature-variant α -TCT after irradiation

The irradiated S79 and S52 have been re-tested in the cryostat after irradiation. The aim is to observe how their pulse shapes change with decreasing temperature, in particular the decaying top of the pulses, as shown in figure 1.16. The decay time gives information on trapping of charge carriers while travelling through the diamond bulk. A variation of the decay time constant as a function of temperature might help to reveal the type and energy level of the charge traps. To observe these effects, a number of requirements have to be met. First, the diamond samples are intentionally not primed prior to the experiment because priming would improve the pulse shapes and change the decay time constant of the signal. Second, keeping in mind that the pulse shape of irradiated diamonds changes with time, the duration of the measurement of an individual data point has to be short – of the order of 30 seconds. Last, the sequence of the bias voltage settings is important, the reason for which is explained below. Temporal pulse changes are unavoidable. For instance, one measurement point takes approximately one minute. After the measurement, the bias voltage polarity is swapped for a few seconds to bring the diamond back into its initial state. A few seconds with respect to a minute is not enough, but due to time constraints this cannot be avoided. Therefore when the bias voltage is set to the next value, there is still some residual effect of the previous measurement. Similar to the effects of polarisation,

480 this effect is also decreasing the pulse height. This can be observed in figure 1.16, which
481 shows the resulting pulses of S52 for bias voltages of ± 200 V, ± 300 V, ± 400 V and ± 500 V
482 at 230 K and 260 K. In this case the measurement sequence is: 230K (200 V, 300 V, 400 V,
483 500 V, -500 V, -400 V, -300 V), 260 K (-200 V, -300 V, -400 V, -500 V, 500 V, 400 V,
484 300 V). The changes in pulse shapes for holes at 230 K and 260 K cannot be attributed
485 to the temperature change. Instead, the explanation lies in diamond polarisation. This
486 means that, when exposed to an electric field with α measurements ongoing, an internal
487 electric field of inverse polarity builds up in the diamond, which effectively reduces the
488 overall electric field. This internal field does not dissipate when the external bias voltage is
489 switched off. The diamond becomes polarised. When switching the polarity of the external
490 bias voltage, the internal and external electric field point in the same direction at the
491 beginning, increasing the overall electric field and with it the pulse height. In figure 1.16
492 this happens when switching from 500 V (figure 1.16a) to -500 V (figure 1.16b) at 230 K.
493 The built up polarisation contributes to the pulse having a sharp rising edge and a high
494 amplitude. This effect decays during the next two voltage points. There are a handful of
495 ways to avoid this polarisation effect in the data:

- 496 1. After every data point invert the bias voltage and leave it to return to a neutral state
497 for the same amount of time,
- 498 2. Make a hysteresis of data points, going from minimum negative to maximum positive
499 bias several times,
- 500 3. Reduce the measurement time at every bias voltage setting.

501 Options (1) and (2) are very time consuming and would increase the overall experiment
502 time significantly. The third option would worsen the resulting averaged pulses. Finally
503 an alternative option has been chosen: alternating the starting bias voltage polarity and
504 the sequence of bias voltages at every temperature point. With this option, a minimum
505 systematic error in analysing the pulse shapes is attained.

506 Figure 1.17 shows the irradiated S52 and S79 as well as the non-irradiated S37 for
507 comparison, all at a bias voltage of ± 500 V and at several temperature points between 4 K
508 and 295 K. It is evident that radiation damage affects the shape of the pulses by means of
509 charge trapping across all temperatures.

1.4. TEMPERATURE LIMITATIONS

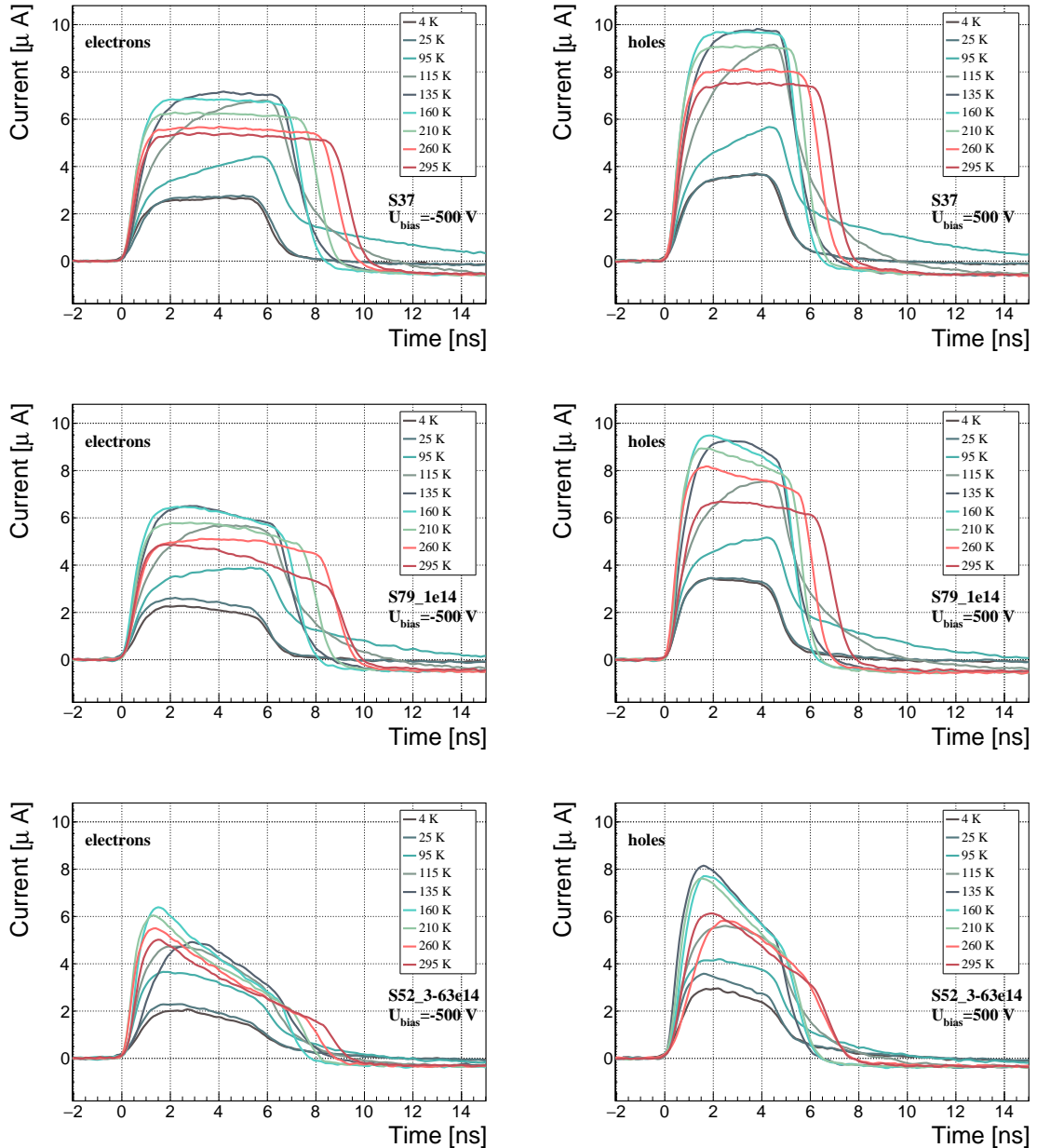


Figure 1.17: Non-irradiated S37 and irradiated S79 and S52. Several data points between 4 K and 295 K at a bias voltage of ± 500 V.

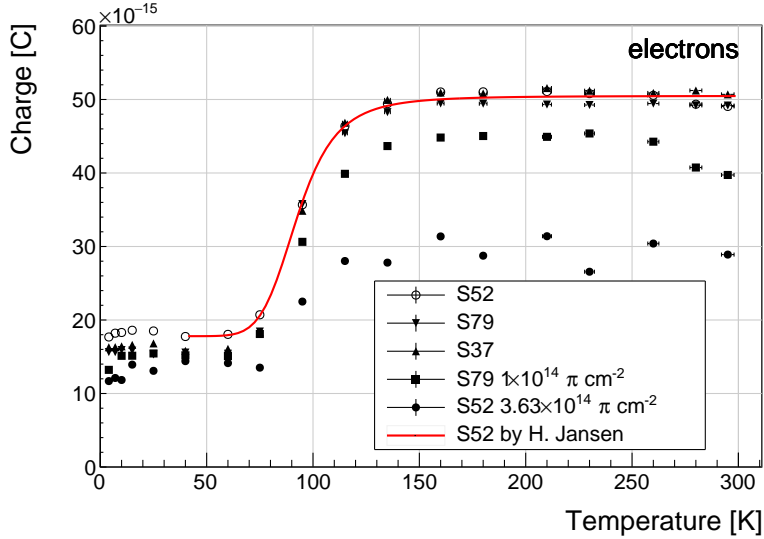


Figure 1.18: Collected charge for electrons as a function of temperature.

510 Collected charge as a function of temperature

511 The collected charge as a function of temperature for electrons and holes is plotted in
 512 figures 1.18 and 1.19, respectively. The red line shows the results from [5]. The new contribu-
 513 tion are the data points for the irradiated samples. The focus is on the temperature range
 514 between 4–75 K and 150–295 K whereby the creation/decay of excitons is not dominating
 515 the pulse shapes. The values for all samples are fairly stable in the range between 4 K and
 516 75 K and between 150 K and 295 K. However, in the values for the irradiated S52 some
 517 excursions can be observed. This is due to the sequence of the measurement steps, which
 518 results in a hysteresis effect explained in the preceding text.

519 The collected charge drops significantly from 150 K down to 75 K. In the non-irradiated
 520 samples the values in the lower temperature range are approximately 30 % of those in the
 521 high range. For the irradiated samples this difference is lower: 35 % for S79 and 50 % for
 522 S52.

523 The highest two temperature points of the S79 are lower due to a change in the mea-
 524 surement setup.

525 An interesting detail in figure 1.18 is that the ratio between the values for non-irradiated
 526 samples and their irradiated counterparts at the lower temperature range is different than
 527 at the higher range. In other words, the charge loss due to irradiation damage is lower for
 528 temperatures between 4 K and 75 K than for temperatures between 150 K and 295 K. The
 529 irradiated S52 collects 78 % of the initial charge in the low temperature range, but only 59 %
 530 of the initial charge for the high range. The values for S79 for these two temperature ranges
 531 are 100 % and 90 %, meaning that the drop in charge collection efficiency after irradiation
 532 to $1 \times 10^{14} \pi \text{ cm}^{-2}$ is negligible for temperatures below 75 K. To sum up, charge trapping is
 533 present in irradiated samples across the entire temperature range, which is evident from the

1.4. TEMPERATURE LIMITATIONS

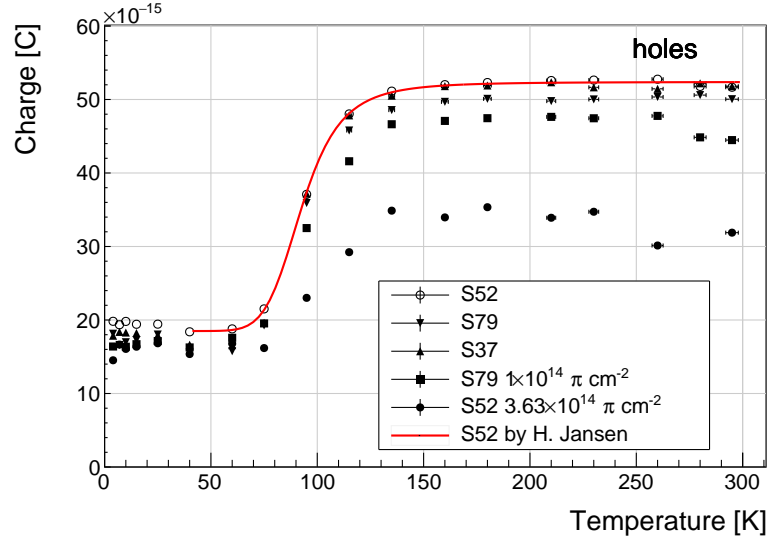


Figure 1.19: Collected charge for holes as a function of temperature.

534 pulse shapes. However, the effect on overall collected charge is reduced for temperatures
 535 between 4 K and 75 K.

536 Charge trapping

537 A decaying exponential function from equation ?? has been fitted to the decaying top of the
 538 averaged pulses at a bias voltages of ± 400 V and ± 500 V across all temperatures excluding
 539 the transitional range between 75 K and 150 K. The resulting decay time constants τ are
 540 effective carrier trapping times. The values differ for individual temperature points due to
 541 changing pulse shapes with time by means of polarisation. This counts as a systematic error.
 542 Therefore the fitted τ for ± 400 V and ± 500 V are averaged into one value representing the
 543 measurement at that temperature point. The time constants should be infinite for an ideal
 544 and non-irradiated sample.

545 As seen in figures 1.20a and 1.20b, the fitted values of the irradiated samples are fairly
 546 stable across all temperatures. There is a slight increase in the decay time constant of the
 547 S52 from $(6.0 \pm 0.5) \times 10^{-9}$ s above 150 K to $(8.5 \pm 0.9) \times 10^{-9}$ s below 75 K. This step is
 548 however not observable in the S79 data. With only one sample exhibiting this behaviour,
 549 the effect is not significant. Judging by the data acquired, the samples would need to be
 550 irradiated to doses above $5 \times 10^{14} \pi \text{ cm}^{-2}$ to quantify this effect in detail. Building on
 551 this assumption, the conclusion is that the signal decay time constant for irradiated sCVD
 552 diamond is constant across the temperature range between 4 K and 295 K, excluding the
 553 transitional range between 75 K and 150 K where it cannot be quantified properly. All
 554 things considered, the values can be averaged into one single effective trapping time value
 555 for electrons and one for holes for further analysis. The effective trapping time is inversely

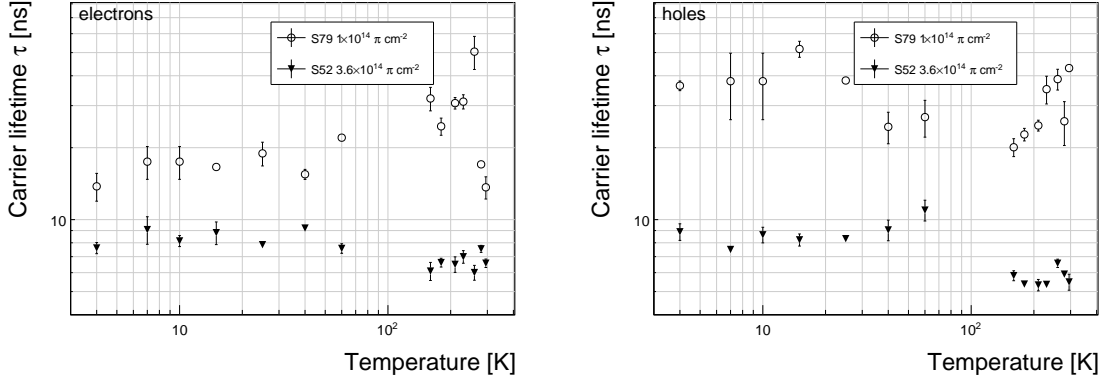


Figure 1.20: Charge carrier lifetime as a function of temperature for electrons and holes at ± 400 V and ± 500 V. The data points between 75 K and 150 K are omitted.

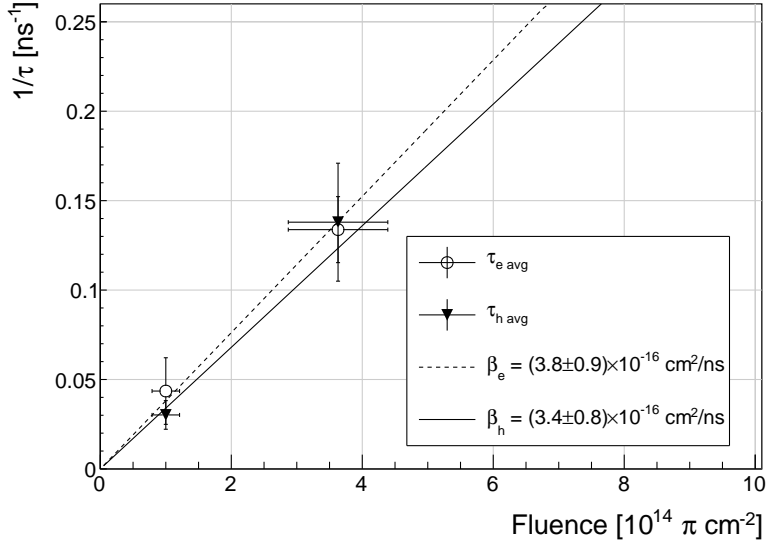


Figure 1.21: This figure shows the inverse charge trapping times averaged over all temperatures and plotted as a function of the π fluence.

556 proportional to the fluence [16]:

$$\frac{1}{\tau} = \beta \cdot \Phi \quad (1.8)$$

557 where β is the proportionality factor. A low β value would mean that the trapping centres
558 in the sensor are created with a low rate. Figure 1.21 shows the inverse trapping times
559 of the non-primed irradiated samples as a function of $\pi_{300 \text{ MeV}}$ fluence. β is the slope
560 of the fitted linear function. The fitted factors are $\beta_e = (3.8 \pm 0.9) \times 10^{-16} \text{ cm}^2/\text{ns}$ and
561 $\beta_h = (3.4 \pm 0.8) \times 10^{-16} \text{ cm}^2/\text{ns}$. Comparing to silicon detectors in [16], the value for the
562 sCVD diamond is two times lower, meaning that it takes twice as much irradiation to create
563 the same amount of charge traps in diamond than in silicon.

564 **1.5 Conclusion**

565 This chapter gives an overview of the capabilities and limitations of diamond as a particle
566 detector. Two effects on diamond are studied – radiation and temperature.

567 Two sCVD diamond detectors were irradiated with 300 MeV pions. They were tested
568 alongside a non-irradiated sample to observe the changes in the ability to detect α , β and
569 γ radiation. Their charge collection efficiency was measured in a test beam facility. The
570 results were compared to the results from the RD42 collaboration and a DPA model. A
571 radiation damage factor $k_\lambda = (4.4 \pm 1.2) \times 10^{-18} \mu\text{m}^{-1} \text{cm}^2$ was obtained for $\pi_{300 \text{ MeV}}$
572 particles. The data point was not in agreement with the data provided by RD42 nor with
573 the model. Most likely this is because there was no diamond surface treatment done in
574 between the measurements, as is the case in the study conducted by RD42. The results
575 obtained in the course of these measurements are going to be fed into the existing pool of
576 data in the RD42 collaboration.

577 The next step was to test the long-term capabilities for α detection. The shape of the
578 ionisation profile was investigated to determine the behaviour of the charge carriers in the
579 irradiated diamond. An exponential decay was observed in the pulses of irradiated samples,
580 proving that there are charge traps in the bulk that were created during irradiation. Then
581 a long-term stability test was carried out. The results show that the irradiated diamond
582 detectors do not provide a stable and reliable long-term measurement of α particles. This
583 might be due to a space-charge build-up in the bulk, which changes the electric field,
584 affecting the charge carriers. A procedure to improve the pulse shape using β and γ radiation
585 was proposed.

586 Finally, the diamond sensors were cooled down to temperatures between 4 K and 295 K.
587 Their response to α particles was observed. The results of the non-irradiated and irradiated
588 samples were compared. The effect of reduction for the number of drifting charges due to
589 exciton creation was observed in both sets of data. The second set had a superimposed
590 effect of charge trapping during the drift, which was represented by an exponential decay
591 in the signal. The decay time constant did not change with temperature. Therefore all
592 temperature points for individual samples were averaged and the decay time constants
593 were plotted as a function of fluence. Proportionality factors for defect production rate
594 $\beta_e = (3.8 \pm 0.9) \times 10^{-16} \text{ cm}^2/\text{ns}$ and $\beta_h = (3.4 \pm 0.8) \times 10^{-16} \text{ cm}^2/\text{ns}$ for non-primed
595 diamonds were extracted.

⁵⁹⁶ Bibliography

- ⁵⁹⁷ [1] *Element Six*. <http://www.e6.com>.
- ⁵⁹⁸ [2] *IHa Technologies Pte. Ltd.* <https://www.2atechnologies.com>.
- ⁵⁹⁹ [3] M. Červ, P. Sarin, H. Pernegger, P. Vageeswaran, and E. Griesmayer. *Diamond de-*
⁶⁰⁰ *tector for beam profile monitoring in COMET experiment at J-PARC*. *Journal of*
⁶⁰¹ *Instrumentation*, 10(06):C06016, 2015.
- ⁶⁰² [4] *DRS4*. <https://www.psi.ch/drs/evaluation-board>.
- ⁶⁰³ [5] Hendrik Jansen, Norbert Wermes, and Heinz Pernegger. Chemical Vapour Deposition
⁶⁰⁴ Diamond - Charge Carrier Movement at Low Temperatures and Use in Time-Critical
⁶⁰⁵ Applications. PhD thesis, Bonn U., Sep 2013. Presented 10 Dec 2013.
- ⁶⁰⁶ [6] *Paul Scherrer Institute*. <https://www.psi.ch/>.
- ⁶⁰⁷ [7] Giorgio Brianti. SPS North Experimental Area. Technical Report CERN-SPSC-T-73-8.
⁶⁰⁸ LabII-EA-Note-73-4, CERN, Geneva, 1973.
- ⁶⁰⁹ [8] Michal Pomorski. Electronic properties of single crystal cvd diamond and its suitability
⁶¹⁰ for particle detection in hadron physics experiments. *Wolfgang von Goethe University,*
⁶¹¹ *Frankfurt am Main, Germany*, 2008.
- ⁶¹² [9] M. Mikuž. *Diamond sensors for high energy radiation and particle detection*. TIPP,
⁶¹³ 2011.
- ⁶¹⁴ [10] V. Sarin. Comprehensive Hard Materials. Elsevier Science, 2014. p. 411.
- ⁶¹⁵ [11] E. Griesmayer and B. Dehning. *Diamonds for Beam Instrumentation. Physics Procedia*,
⁶¹⁶ 37:1997 – 2004, 2012. Proceedings of the 2nd International Conference on Technology
⁶¹⁷ and Instrumentation in Particle Physics (TIPP 2011).
- ⁶¹⁸ [12] V Eremin, E Verbitskaya, and Z Li. Effect of radiation induced deep level traps on si
⁶¹⁹ detector performance. *Nuclear Instruments and Methods in Physics Research Section*
⁶²⁰ *A: Accelerators, Spectrometers, Detectors and Associated Equipment*, 476(3):537 – 549,
⁶²¹ 2002. Proc. of the 3rd Int. Conf. on Radiation Effects on Semiconductor Materials,
⁶²² Detectors and Devices.

BIBLIOGRAPHY

- 623 [13] S. F. Kozlov, R. Stuck, M. Hage-Ali, and P. Siffert. Preparation and characteristics of
624 natural diamond nuclear radiation detectors. *IEEE Transactions on Nuclear Science*,
625 22(1):160–170, Feb 1975.
- 626 [14] Eugenijus Gaubas, Tomas Ceponis, Dovile Meskauskaitė, and Nikolai Kazuchits. Pro-
627 filing of current transients in capacitor type diamond sensors. *Sensors*, 15(6):13424,
628 2015.
- 629 [15] Gregor Kramberger, V. Cindro, A. Gorisek, I. Mandic, M. Mikuz, and M. Zavrtanik.
630 *Effects of bias voltage during priming on operation of diamond detectors*. PoS, Ver-
631 tex2012:013, 2013.
- 632 [16] Alison G. Bates and Michael Moll. A comparison between irradiated magnetic czechral-
633 ski and float zone silicon detectors using the transient current technique. *Nuclear In-*
634 *struments and Methods in Physics Research Section A: Accelerators, Spectrometers,*
635 *Detectors and Associated Equipment*, 555(12):113 – 124, 2005.